In: AIAA Aviation Forum and Ascend 2025, 21-25 July 2025, Las Vegas, Nevada, Article number AIAA 2025-3198
DOI: 10.2514/6.2025-3198

Supersonic Projectile Flow Field Reconstruction using Background-Oriented Schlieren and Physics Informed Convolutional Neural Networks

Miguel A. Escudero*
Royal Military Academy, Brussels, 1000, Belgium
Centre for Defence Engineering and Physical Science, Cranfield University, Defence Academy of the UK, Shrivenham SN6 8LA, Oxfordshire, UK

Benoît G. Marinus†
Royal Military Academy, Brussels, 1000, Belgium

Karthik Depuru-Mohan‡
Centre for Defence Engineering and Physical Science, Cranfield University, Defence Academy of the UK, Shrivenham SN6 8LA, Oxfordshire, UK

Marco Debiasi§
Centre for Defence Engineering and Physical Science, Cranfield University, Defence Academy of the UK, Shrivenham SN6 8LA, Oxfordshire, UK

Alistair J. Saddington¶
Centre for Defence Engineering and Physical Science, Cranfield University, Defence Academy of the UK, Shrivenham SN6 8LA, Oxfordshire, UK

This work explores the use of axisymmetric background-oriented schlieren (BOS) imaging for reconstructing supersonic flow fields over a scaled NATO 5.56 mm M855 projectile at Mach 1.50, 2.00, and 2.50, as well as a 15° cone at Mach 2.50. A method for recovering density fields from BOS displacement maps was implemented, with results compared to a Taylor–Maccoll solution for the cone and a RANS CFD wind tunnel model for the projectile. Density field reconstructions showed errors below 15% overall and under 10% across most of the field, with the largest deviations near shock boundaries and stagnation regions. Additionally, force balance measurements were conducted on the projectile at Mach 2.50, showing an agreement of 1.2% with firing data from the literature and 8% with the RANS model. A custom U-Net was subsequently trained to predict pressure, temperature, and velocity fields from grid-transformed numerical density inputs over the cone, using a physics-exclusive loss function derived from the Euler conservation laws and specified boundary conditions. However, large residuals near the shock and stagnation point due to grid interpolation were found to impede the network's performance. A purely data-driven model demonstrated good accuracy for pressure and temperature, a moderate performance for radial velocity, and poor accuracy for axial velocity. The model failed to generalize when fed with experimental data, reinforcing the need for strong physical constraints.

*PhD student in a joint framework between RMA and Cranfield University, Department of Mechanical Engineering, avenue de la Reinassance 30
†Professor, Department of Mechanical Engineering, avenue de la Renaissance 30, AIAA senior member
‡Lecturer, Centre for Defence Engineering and Physical Science, Cranfield University, The Defence Academy of the UK, Shrivenham SN6 8LA, United Kingdom, AIAA senior member
§Research Fellow,Centre for Defence Engineering and Physical Science, Cranfield University, The Defence Academy of the UK, Shrivenham SN6 8LA, United Kingdom
¶Professor,Centre for Defence Engineering and Physical Science, Cranfield University, The Defence Academy of the UK, Shrivenham SN6 8LA, UK

Published by AIAA. This is the Author Accepted Manuscript issued with: Creative Commons Attribution License (CC:BY 4.0).
The final published version (version of record) is available online at DOI:10.2514/6.2025-3198. Please refer to any applicable publisher terms of use.

I. Nomenclature

BOS	=	Background-oriented schlieren
CNN	=	Convolutional Neural Network
GCI	=	Grid Convergence Index
GELU	=	Gaussian Error Linear Unit
MSE	=	Mean squared error
PINN	=	Physics Informed Neural Network
PI-CNN	=	Physics Informed Convolutional Neural Network
RANS	=	Reynolds Averaged Navier-Stokes
SBLI	=	Shockwave-Boundary-Layer Interaction
f	=	Lens focal length
h	=	Camera sensor height
n	=	Refractive index
R	=	Flow field radius
r	=	Radial coordinate in physical space
T	=	Fluid temperature
u	=	Axial component of fluid velocity
v	=	Radial component of fluid velocity
w	=	Camera sensor width
x	=	Axial coordinate in physical space
y	=	Vertical coordinate in physical space
γ	=	Ratio of specific heats
ρ	=	Fluid density
θ	=	Angular coordinate in the shockwave's reference frame
ξ	=	Axial coordinate in computational space
η	=	Radial coordinate in computational space
C_D	=	Drag coefficient
$C_{D,\text{extrp}}$	=	Extrapolated zero-yaw drag coefficient to zero discretisation error
$C_{D,\text{exp}}$	=	Experimental zero-yaw drag coefficient
M_∞	=	Freestream Mach number
N_{int}	=	Number of interior points
N_{bc}	=	Number of boundary points
n_0	=	Refractive index of light in the freestream
R_x	=	Picture horizontal resolution
R_y	=	Picture vertical resolution
r_{mesh}	=	Mesh refinement ratio
r_{surf}	=	Radial coordinate along cone surface
$V_r^{'}$	=	Normalised radial velocity component in the shockwave's reference frame
V_∞	=	Freestream velocity
Z_c	=	Distance between camera lens and flow plane
Z_d	=	Distance between reference pattern and flow plane
ϵ_{approx}	=	Average error between values from different meshes
$\epsilon_{\text{extrapolated}}$	=	Extrapolated error between values from different meshes
ϵ_{approx}	=	Approximate relative error
ϵ_{extrp}	=	Extrapolated relative error
ϵ_x	=	Angle of axial light ray deflection
ϵ_y	=	Angle of radial light ray deflection
ϕ_∞	=	freestream value of quantity ϕ
$\phi^\star$	=	freestream normalised value of quantity ϕ
θ_c	=	Cone angle
θ_s	=	Shock angle
x/L	=	Non-dimensional axial coordinate relative to projectile/cone length
r/R	=	Non-dimensional radial coordinate relative to projectile/cone diameter

II. Introduction and Objectives

A. Introduction

External ballistic calculations are crucial to understanding and predicting the dynamics of projectiles [1]. Such dynamics are strongly determined by the aerodynamic forces and moments acting on the projectiles during flight, influencing their precision, range, and stability [2]. The aerodynamic coefficients of a projectile are typically obtained in ballistic range experiments [3–5], however, the unsteady nature of these flows make it difficult to examine specific conditions with high accuracy, generally presenting a large spread in results [6]. Alternatively, more repeatable conditions may be achieved using high-speed wind tunnels. Nevertheless, scaling effects such as sting interference, blockage, and shock reflections must be correctly accounted for and understood [7]. Furthermore, the force sensors that are traditionally used in these applications [8], may impose experimental constraints in terms of minimum model size and usable test section size, which can be problematic in smaller wind tunnels.

Instead, the strong density gradients that are characteristic of supersonic flows may be exploited for quantitative measurement through optical techniques, such as background-oriented schlieren (BOS) [9, 10]. Unfortunately, only density fields may be reconstructed from standard BOS measurements, whereas additional information, such as pressure, is necessary to infer aerodynamic forces. To expand on this technique, emerging machine learning models have been applied to different fluid mechanics applications.

One of the most popular approaches is the use of Physics Informed Neural Networks (PINNs) [11] which implement the governing physical laws directly into the network's cost function. PINNs have been directly applied to high-speed flow cases [12], successfully obtaining pressure and velocity fields from two-dimensional oblique shock density gradient data, using the Euler equations and discrete pressure measurements to create training penalties. Other uses of the Euler equations include the work in [13], with additional irrotationality constraints for BOS image pairs from the axisymmetric cone and expansion fan experiments. More recent efforts have used the Reynolds Averaged Navier Stokes (RANS) governing equations, successfully recovering pressure and velocity information for an underexpanded turbulent jet [14] and hypersonic bluff bodies [15]. Further additions to the physics constraints, such as measured wall pressure distributions or wall shear stress conditions have been shown to be key in predicting separating flows in shock boundary layer interactions (SBLI) and boundary layer profiles accurately [16].

Moreover, the image-to-image regression nature of mapping density fields to other flow quantities has also inspired the application of Convolutional Neural Networks (CNNs). Recent works have employed CNNs in BOS data pre-processing, enabling super-resolution in displacement field refinements [17], and fast, high accuracy, pixel resolution displacement field calculations from image pairs with imposed irrotationality constraints [18]. In terms of flow-field reconstruction, CNNs may leverage the advantage of the physics-based loss functions from fully connected PINNs, while extending to higher-dimensional problems and benefitting from parameter sharing and local connections [19]. This was exemplified in [19], where a physics-informed CNN was used to predict a steady-state temperature field from a heat source layout, in [20] for Darcy flows, or in [21] for the incompressible Navier-Stokes using grid transformations.

B. Objectives of the Research

The primary objective of this research is to evaluate the feasibility of using BOS imaging to reconstruct density fields around axisymmetric bodies, focusing on two canonical cases: a sharp cone at angle of attack and a scaled small-caliber supersonic projectile. The study aims to identify regions where BOS measurements are prone to higher errors, particularly near steep flow gradients or zones with low pixel displacement sensitivity, and to assess which flow features present the greatest challenge for accurate reconstruction. Secondly, we aim to investigate the use of physics-informed convolutional neural networks (PI-CNNs) to recover full flow fields from BOS-derived density inputs. This includes evaluating how well PI-CNNs trained on numerical (CFD) data generalize to experimental data, and where discrepancies arise.

The end goal of this research seeks to develop a fully integrated workflow that combines CFD, wind tunnel simulations, physics informed machine learning models, and experimental BOS and force sensor data to predict a projectile's zero-yaw drag coefficient over a range of supersonic Mach numbers.

III. Methodology

A. Experimental Methodology

1. Wind Tunnel Facility

The experiments were carried out at the UK Defence Academy's 150 × 150 mm blowdown supersonic wind tunnel. The tunnel was supplied with dry air by an L110-10 Compair compressor, and stored in a pressure reservoir at an absolute pressure of 6.75 bar. The nozzle geometry was modified manually using mechanical actuators to achieve nominal test section Mach numbers of 1.5, 2.0, and 2.5.

2. Background-Oriented Schlieren Measurements

The setup for the BOS measurements is shown in Figure 1, where the wind tunnel test section is rotated around its axis by 90° better to show the window's location and the model arrangement. For image capture, a 26.1-megapixel Fujifilm X-T30 II camera with a 70-210 mm f/3.5-4 macro lens was used. The camera was supported by a tripod with the lens axis perpendicular to the test-section window and at the same height as the projectile centerline. The BOS reference pattern was generated using a random distribution of circular dots and placed on the opposite side of the test section relative to the camera. The pattern was stretched between two aluminium frames mounted on a tripod whose head orientation and height were adjusted to maintain the frame parallel and at the same height as the test-section window. A plexiglass pane was used to shield the pattern to avoid its deformation by any spurious stream of air in the room. The measurement parameters are summarised in Table 1.

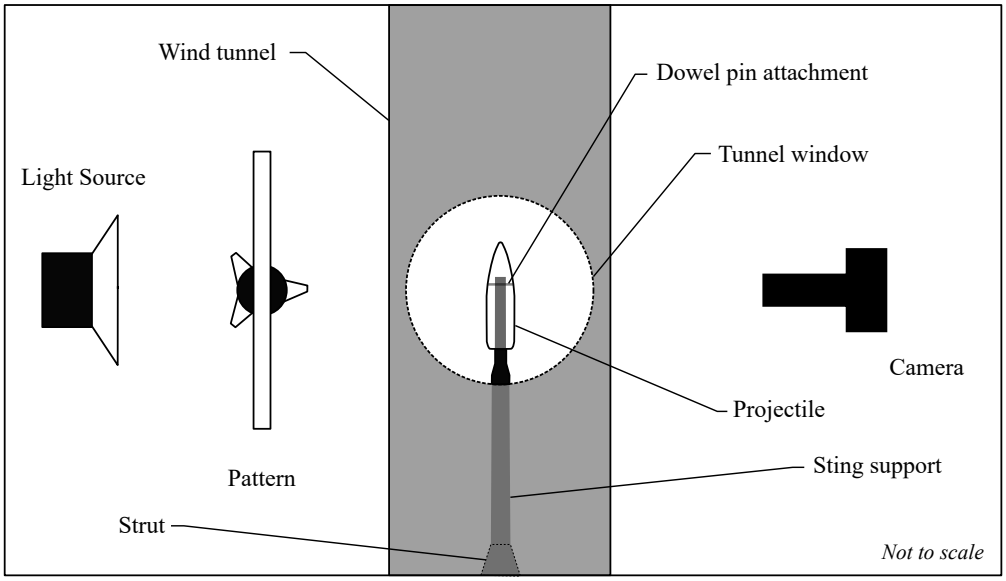

Fig. 1 Bird's-eye view diagram of the BOS setup; the wind tunnel test section is rotated 90° to show the window's location and the model arrangement.

Table 1 Measurement parameters for BOS experiments

Z_c, mm	Z_d, mm	f, mm	w, mm	h, mm	R_x, pix	R_y, pix
1250	390	105	23.5	15.6	6240	4160

3. Wind Tunnel Models

In this work, we consider two different model geometries, Figure 2. The first one is a canonical cone-cylinder geometry [22] that is used as a reference case for the BOS set-up in our initial experiments. This consists of a cylindrical body whose diameter and length are 21 mm and 87.5 mm, respectively with a 39.2 mm long conical nose (for a cone

angle of 15°, i.e. a tip angle of 30°). The base of the steel-made model was screw-mounted on a sting support projecting forward from a strut located in the middle of the wind tunnel diffuser. The second model is a 4.5:1 scale NATO 5.56 mm M855 projectile [4], manufactured from polyoxymethylene (POM) plastic. This model incorporates a 15 mm opening through its base where a sting balance or, alternatively, its dummy equivalent is inserted by means of which the model is mounted on the projecting sting support.

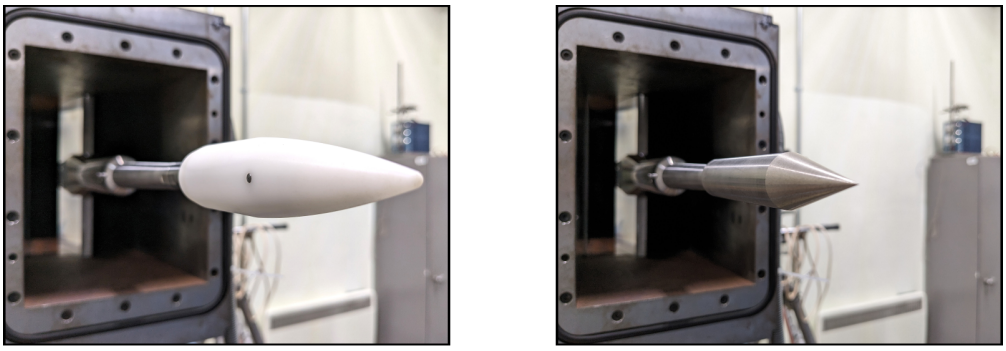

(a) (b)

Fig. 2 Wind tunnel models (a) 4.5:1 scale NATO 5.56 mm M855 (b) cone-cylinder geometry

4. Force Balance Measurements

An Aerotech 6-component sting balance was used to measure the drag of the projectile model. The balance was connected to the projectile through the base opening that terminates with a 12 mm cylindrical hole snugly fitting around the tip of the balance. Their relative position was secured by a dowel pin passing through the body of the projectile and the tip of the balance, shown in Figure 1. The balance's design load ranges are ±100 N for drag and side forces, ±200 N for lift, ±2 Nm for the rolling moment and ±4 Nm for the pitch and yaw moments. Although steady state forces were well within the balance's limits, large peaks of the yawing moment were measured during start-up and end-of-test ramp-down that reached the corresponding overload values and thus limited the use of the balance only to the Mach 2.50 case. The balance's strain-gauge voltages were recorded at a sampling frequency of 1 kHz by a Dewetron NEX[DAQ] data acquisition system and converted to force and moment values according to the balance calibration data.

B. Numerical Approach

1. Computational Fluid Dynamics

A 3D RANS CFD model was built using the commercial software Star-CCM+ 2306 [23], for direct comparison with the experimental flow field and force measurements. The computational domain was simplified to a quarter model, shown in Figure 3, as per the axisymmetric nature of the flow considered. The model extends from the stagnation chamber interface down to three projectile lengths aft of the projectile's base, as any further extension was shown not to affect the upstream field. The flow inlet was modelled using a stagnation boundary condition, where the reservoir's air pressure and temperature were set to match the compressor settings during experiments. The nozzle geometry was modified to achieve the desired test-section Mach number, following the wind tunnel's engineering drawings. The outlet temperature and pressure were calculated using the isentropic flow relations, and the inlet stagnation pressure and measured test section Mach number. All remaining non-symmetrical boundaries were assigned as no-slip walls. The flow turbulence was modelled using the $k-\omega$ SST model [24], with no-slip walls meshed to obtain y^+ values around 1, as per the model's recommendation [23]. The turbulence model was chosen for its superior performance in handling adverse pressure gradients, expected to form across shockwave reflections, compared to other methods typically used in similar cases, like the Spalart-Allmaras model [25]. The mass, momentum, and energy conservation equations were solved using the coupled flow and energy methods. A third-order MUSCL discretization scheme was employed to treat cell face convection and diffusion fluxes, as this was seen to better capture shock structures and Liou's AUSM+ Flux-Vector Splitting (AUSM+ FVS) scheme was used to manage the inviscid fluxes [26]. All solutions were

initialised with the built-in grid-sequencing method. To further increase convergence speed, automatic Courant number control was employed for the implicit pseudo-time stepping as well as the continuity convergence accelerator.

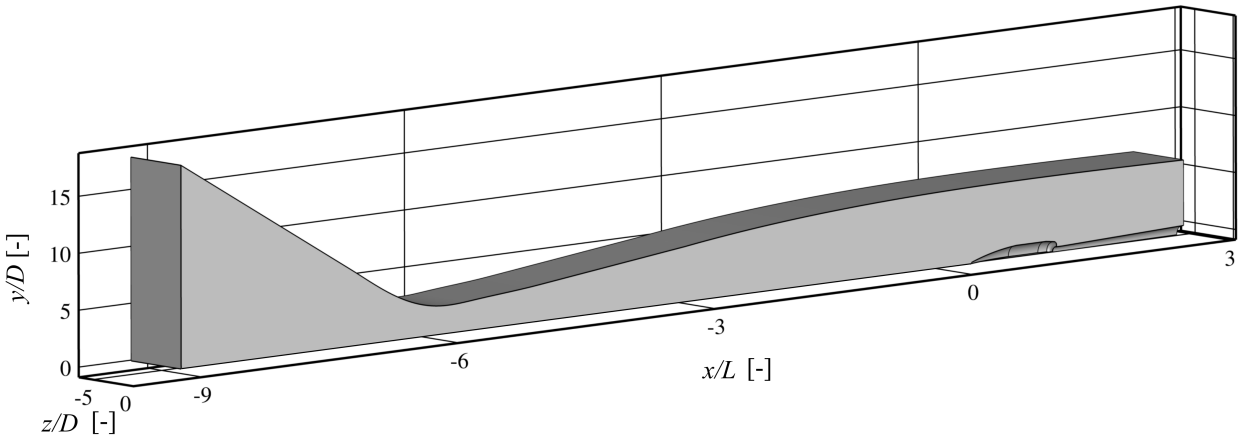

Fig. 3 Computational domain of the 3D RANS model

2. Density Field Reconstruction

Sets of reference/flow-off and flow-on image pairs were processed using OpenCV's library implementation of the Gunnar-Farneback optical flow algorithm[27, 28] in Python. The algorithm allows for the computation of the observed pixel shifts in the background pattern due to the light source rays refracting through the compressible air. These were then related to the refractive index gradients using modified inverse Abel transforms [29]:

$$\epsilon_x(x,y) = \frac{2}{n_0}\int_{r=y}^{R} \frac{\partial n}{\partial x}\frac{r\,dr}{\sqrt{r^2-y^2}} \tag{1}$$

$$\epsilon_y(x,y) = \frac{2}{n_0}\int_{r=y}^{R} \frac{\partial n}{\partial r}\frac{r\,dr}{\sqrt{r^2-y^2}} \tag{2}$$

where $\epsilon_x(x,y)$ and $\epsilon_y(x,y)$ represent the angular deflections of the light rays passing through the flow field, n_0 is the refractive index of the freestream air, R is the radius of the flow field, $\frac{\partial n}{\partial x}$ and $\frac{\partial n}{\partial r}$ are the gradients of the refractive index in the radial and axial directions, and y is the coordinate along the projected image plane. The angular deflections can be directly obtained from the pixel displacement maps and the geometrical layout of the setup [30].

The refractive index field, $n(r)$, may be expressed as a series of sinusoidal functions, Eqns. (3) and (4). The coefficients A_n are obtained by substituting Eq. (3) into Eqs. (1) and (2), then least square fitting using the measured, angular displacement matrices [31].

$$n(r) = \sum_{n=N_i}^{N_u} A_n f_n(r) \tag{3}$$

$$f_0(r) = 1,\ f_n(r) = 1 - (-1)^n\ \cos(n\pi\frac{r}{R}) \tag{4}$$

We implement this workflow using an in-house Python code, which employs the Numba Just-in-Time (JIT) compiler library [32], allowing for speed-enhanced, parallelised calculations.

3. Taylor-Maccoll Flow

The flow over the cone portion of the cone-cylinder body is well represented by the Taylor-Maccoll equations for inviscid, compressible, conical flow:

$$\frac{\gamma-1}{2}\left[1-V_r^{'2}-\left(\frac{dV_r^{'}}{d\theta}\right)^2\right]\left[2V_r^{'}+\frac{dV_r^{'}}{d\theta}\cot(\theta)+\frac{d^2V_r^{'}}{d\theta^2}\right]-\frac{dV_r^{'}}{d\theta}\left[V_r^{'}\frac{dV_r^{'}}{d\theta}+\frac{dV_r^{'}}{d\theta}\frac{d^2V_r^{'}}{d\theta^2}\right]=0 \tag{5}$$

where γ is the ratio of specific heats, $V_r^{'}$ is the normalised radial velocity component across the shock wave, and θ is an angular coordinate in the shock plane. We implement the shock-fitting method described in [33] to solve for the shock-relative velocity components as a function of their angular coordinate. This is followed by a reference frame transformation from which the density, pressure, and temperature fields are interpolated on a 256 × 256 numerical grid, shown in Figure 4. The density field predictions were used for comparison with the BOS reconstructed fields and later coupled with pressure, temperature, and velocity for the training of our CNN.

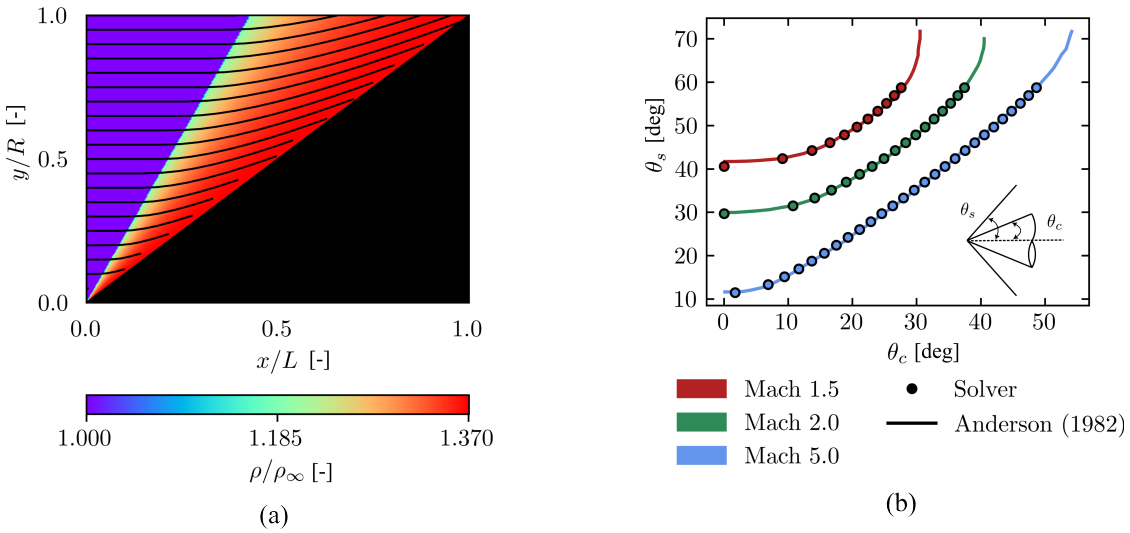

Fig. 4 Taylor-Maccoll flow solver results (a) Mach 2.50 Density field with velocity streamlines over a 15 degree cone (b) Shock angle against cone angle for Mach 1.50, 2.0 and 5.0, compared with and adapted from [33]

4. Convolutional Neural Network

We employ a custom U-Net-style CNN [34] to map normalized input density fields at specific grid coordinates to predicted output pressure, velocity, and temperature results. The architecture is designed for pixel-wise regression on structured axisymmetric domains, representative of projectile or cone bodies at zero yaw. The network is divided into an encoder, bottleneck, decoder, and output head components. The encoder is made up of two convolutional blocks, each comprised of two 2D convolutional layers with 3×3 kernels and Gaussian Error Linear Unit (GELU) activation functions. These map the input tensor into a compressed latent representation. The bottleneck receives the lowest-resolution features using a similar convolutional block to capture the high-level spatial semantics. Next, the decoder upsamples the latent representation through bilinear upsampling followed by 3×3 convolutions. The upsampling stages are followed by convolutional blocks which integrate skip connections from the encoder to preserve spatial detail, eventually restoring the original input resolution. Finally, we use four output heads to separately predict the individual tensor channels, i.e. the predicted flow fields, this way minimising interference between the different magnitude variations between them.

Here we focus on the conical flow case, using a dataset of 1377 simulations as described in Section IV.C.1. The dataset is separated into training and validation sets using an 80/20 stratified split. A batch size of 1 is used as is typical of physics-informed models. The Adam optimizer [35] is employed with a learning rate of 1×10^{-4} and a norm threshold of 1.0 to increase training stability. All models are trained using A100 Nvidia GPUs using the Royal Military Academy's and Cranfield University's high-performance computing clusters, Reynolds and Delta, respectively.

IV. Results

A. General Flow Field

The different flow cases at Mach 1.5, 2.0, and 2.5 are shown in Figure 5. Each result compares an instantaneous, traditional, schlieren visualization with a pixel displacement magnitude map, obtained from two distinct runs of the same experiment. The Mach 2.0 and 2.5 cases were shown to achieve a consistent steady state, through very similar flow features observed in the different runs. On the other hand, the Mach 1.5 flow showed instabilities near the end of the cylinder and boattail of the projectile, visible as separation from the body in the schlieren image. The corresponding BOS displacement contour shows similar features up to the ogive-cylinder junction, beyond which the results differ due to the unsteady flow and different time instants represented.

Generally, the main features captured by the higher contrast traditional Schlieren system are meaningfully replicated by the BOS results, such as the leading bow shock and its adjacent density gradient, the expansion fans around the geometry transitions along the projectile, and the weaker expansions induced by the covered dowel pin holes toward the end of the ogive section. The traditional schlieren system can capture weak density variations, such as those induced by imperfections in the upstream nozzle geometry, which are less discernable in the BOS results. Notably, however, the BOS contours more clearly discriminate the shear layer around the projectile wakes in all cases. The shock reflections on the wind tunnel test section are similarly captured with both methods, and can be seen travelling downstream between the Mach 1.50 and Mach 2.0 cases, eventually leaving the measurement window as the bow shock angles further reduce at Mach 2.50. Additionally, small non-zero pixel shifts are observed in the upstream regions, most noticeably in the Mach 2.0 case. These are caused by shifts in the pattern and/or camera's original relative locations due to vibrations induced by the facility during operation and minor air currents induced in the room.

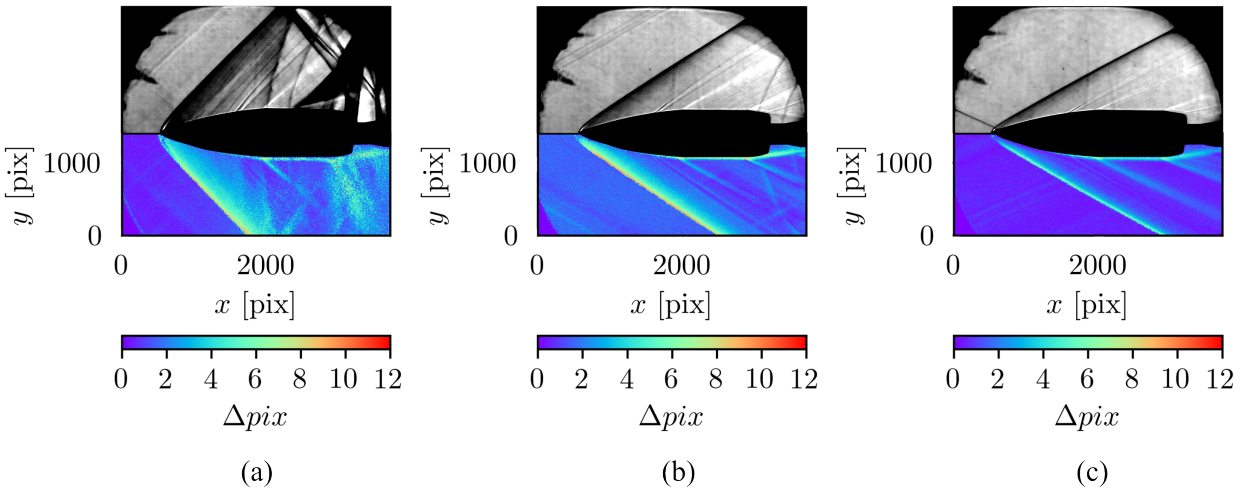

Fig. 5 Comparison of BOS pixel displacements and schlieren images for the 4.5:1 scale NATO 5.56 mm projectile at (a) Mach 1.5 (b) Mach 2 (c) Mach 2.5

The optical flow processing method allows for the decomposition of the pixel displacements into horizontal and vertical components. This is shown for the Mach 2.0 flow case in Figure 6. The separation of components makes it possible to separate flow features such as the bow shock reflections, almost completely accounted for by the horizontal displacements. The vertical displacement contour shows the compression and expansion structures along the windward and leeward sides of the projectile to be qualitatively symmetrical, showing opposite sign deflections for shocks and expansions along either side, as well as opposite sign deflections between equivalent features on the two opposite sides of the projectile. Quantitatively, the edge of the shockwave on the top half of the contour ($y > 285$pix) exhibits larger absolute vertical displacements, of 7-8 pixels relative to the shock edge on the bottom half ($y < 285$pix), with a 6-pixel average shift. Conversely, the expansion fans regions over the bottom projectile surface show a consistent upward shift of 1.5 pixels relative to the top surface displacements. Finally, the flow region adjacent to the top shockwave extends further

downstream by 68 pixels on average or 0.44 projectile diameters. On the other hand, The horizontal displacement map exhibits near-perfect symmetry about the projectile longitudinal axis (y = 285pix), with average shifts of 8 pixels across the bow shock and 0.1-1.2 pixels across the expansion fan, depending on projectile proximity. The displacement magnitude exhibits similar asymmetries to those identified in the vertical shift maps. These are likely caused by small misalignments between the camera lens and the horizontal axis of symmetry, which is further supported by the negligible asymmetry in the horizontal shifts. The component decomposition of the observed pattern displacements can therefore be used in the future to fine-tune the tripod position and this way minimise the error induced by misalignment.

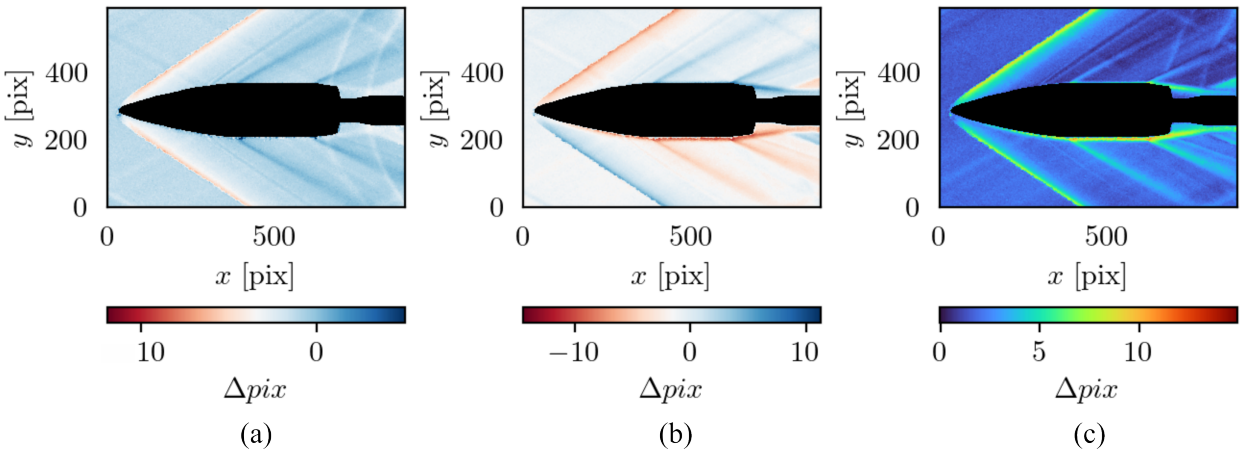

Fig. 6 Pixel displacement maps for the scale x4.5 Nato 5.56 M855 at Mach 2 (a) Horizontal displacement (b) Vertical displacement (c) Magnitude of displacement

Additionally, significant displacements are observed in the near-wall region of the projectile in the displacement magnitude plot. The component decomposition indicates that vertical refractions are the primary contributor, showing the light rays are deflected away from the projectile body. The near-wall displacement regions grow in thickness along the projectile longitudinal axis, in a similar fashion to the boundary layer. However, said thickness is overpredicted by the BOS images when compared with the traditional schlieren images shown in Figure 5. A known limitation of the BOS technique is the model blur which occurs when attempting to bring two separated planes (model plane and pattern plane) into focus equally. Furthermore, flow-induced vibrations on the supports and projectile are equally captured as shifts from the reference image by the optical flow algorithm. Finally, the blurring effects make precise masking of the wall boundaries difficult, resulting in artifacts associated with the highest displacement peaks in both components. The measurement and processing errors introduced in this region warrant careful consideration and difficult further analysis of the boundary layer. On a similar note, the stagnation points are typically misrepresented by low pixel displacements, despite the largest flow compression being expected here. Again, the size of this region is comparable to the blurring around the projectile nose, obscuring the measured deflection.

B. Reconstructed Density Fields

1. Conical Flow

The results for the cone cylinder flow at Mach 2.50 are shown in Figure 7. The pixel displacement magnitude contour plot in 7c exhibits values in a similar range to the projectile experiments described in Section IV.A, with a clear capture of the conical shock, stronger expansion fan, boundary layer-like near-wall region with increasing thickness, and final expansion near the base of the cylinder. Focusing on the cone portion of the model ($650pix < y < 900pix$), Figure 7 presents the processed density field. Overall, the results show good qualitative agreement with the Taylor-Maccoll solution presented in Figure 4, with near unity upstream values, and a clearly delimited shock region with a positive density gradient along the flow direction.

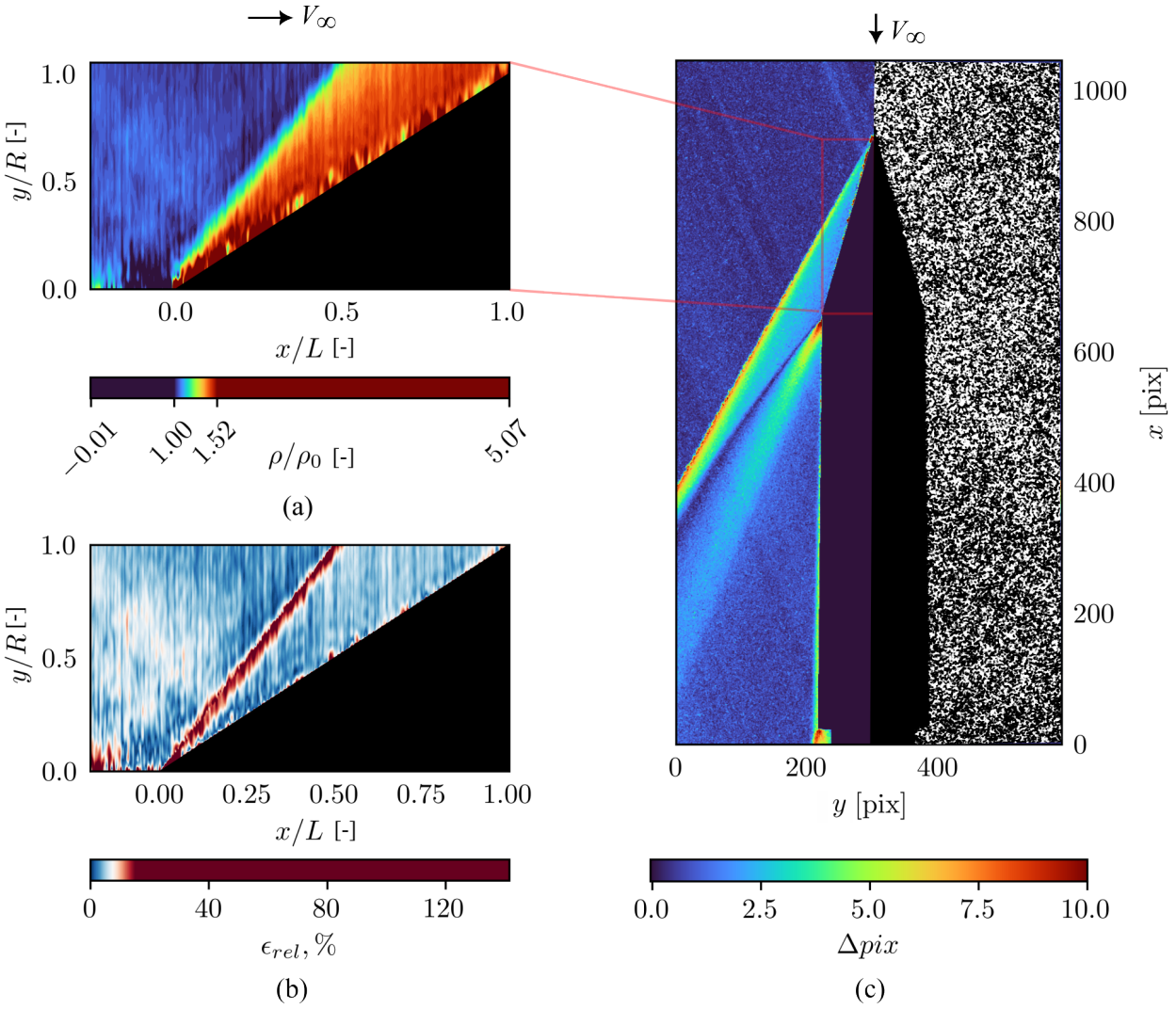

Fig. 7 Cone flow results at Mach 2.5 (a) Contour of BOS reconstructed noramlised density, with colorbar capped at the maximum and minimum predictions from the numerical Taylor-Maccoll solution (b) Relative error between experimental and numerical density fields (c) Pixel displacement magnitude contour for the cone-cylinder flow (left) with BOS random dot pattern used (right)

Noticeably, the shock interface is less sharp than in the calculated solution, which is an expected consequence of the limited camera resolution, BOS flow plane blurring, and windowing effects of the optical flow algorithm. This results in the largest source of error, as identified in Figure 7b. As shown, the pointwise relative error between the Taylor-Maccoll numerical solution and the experimental density field shows a distinct rise in perfect alignment with the shock location, exceeding the 15% error threshold imposed on the contour. Another noticeable spike is visible at the bottom left corner of the contour ($x/L = -0.2$), which is a numerical artifact occurring around the axis of axisymmetry during the integration process. This may be minimised by using finer integration steps, at the cost of additional computational time. Other visible discrepancies occur upstream of the shock, as the experimental flow field captures the shocks created by the imperfections in the upstream nozzle geometry, which are not modelled in the uniform upstream field of the numerical solution. Finally, some near-wall spikes in error are visible due to the artifacts discussed in Section IV.A. Otherwise, the relative error in the resolved field differs by less than 15% at worst, with the majority of the error below 10%.

2. Projectile Flow

Following the cone flow experiments, the projectile pixel displacement maps were processed to yield the experimental density fields. The Mach 1.5, 2.0, and 2.5 flows around the projectile model are shown in Figure 8a-c. The filled contours show the free-stream normalised density fields, over which the RANS model results are overlaid with black contour lines. In all cases, the fields are qualitatively well represented. The shock and expansion locations and orientations are captured, while the filled contours show the gradients in density occurring between the different structures. The shear layer around the wake is visible in both experimental and numerical results for the two higher Mach number cases, although worse agreement is seen for the Mach 1.50 case.

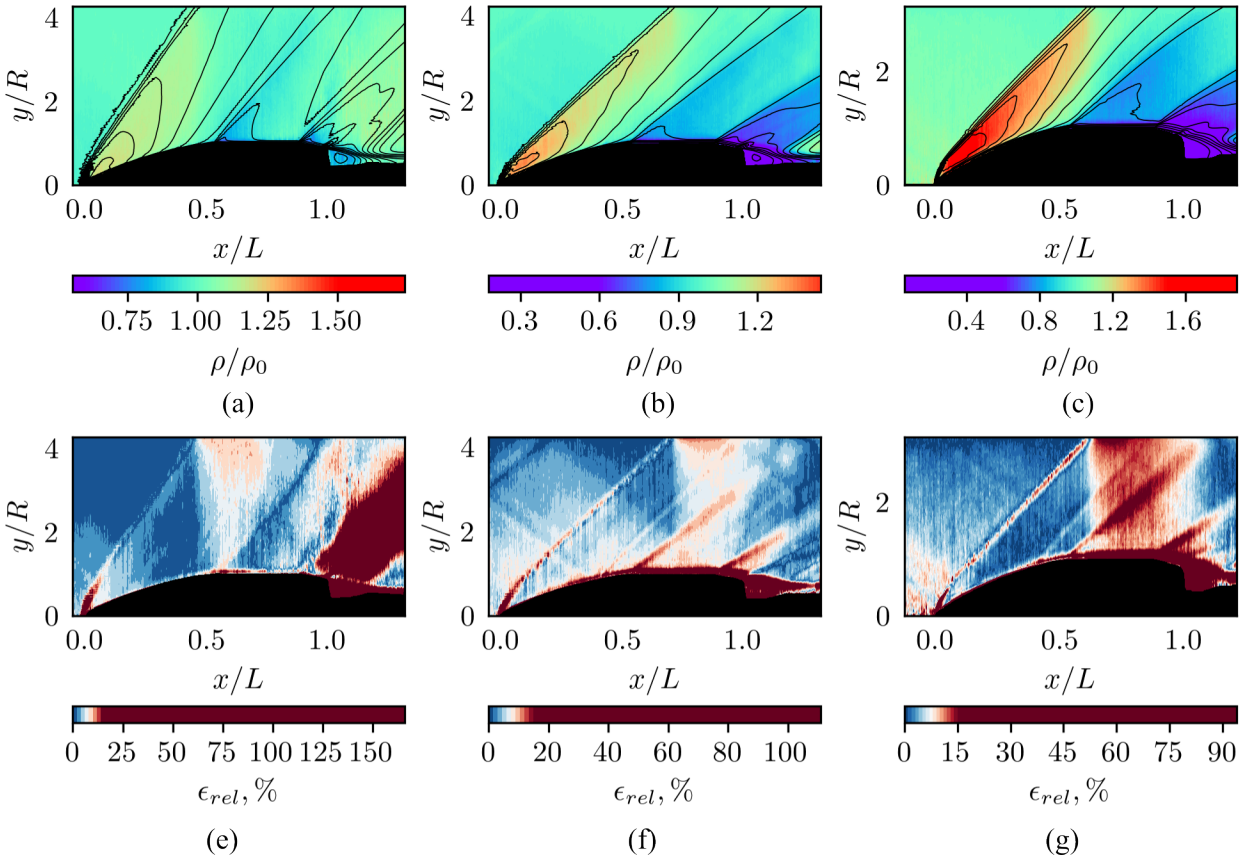

Fig. 8 Normalised denity contours of the flow over a 4.5:1 scale NATO 5.56 M855 projectile. Coloured contours represent experimental BOS result with overlaid CFD contours in black. Flow fields and relative error between experimental and numerical methods are shown for (a),(d) Mach 1.5, (b),(e) Mach 2.0 and (d),(f) Mach 2.5

The plots in 8d-f show a pointwise comparison of the relative error between the experimental results and the CFD results interpolated on an equally sized grid, with contours limited to a maximum absolute error of 15%. Similarly to the conical flow results, the errors spike along the leading shockwave. In this case, however, the error magnitudes are smaller. The shock-fitting Taylor-Maccoll method provides a sharper transition between upstream and compressed flow, whereas the shock-captured solution from the RANS model resembles the smoothed-out shock at the current mesh resolution. The near-wall error region increases with projectile length, differently from the cone example, due to the more developed boundary layers over the longer projectile length. Most notably, large errors also occur along the projectile's base in all cases. Since the near base wake is subsonic, density gradients in this region are orders of magnitude weaker and so the measurement technique struggles to capture the flow density accurately in this region. As expected from the pixel displacement results, the stagnation points are regions of large error in all cases. The density peaks predicted by the CFD models are significantly underpredicted due to the image blur near the projectile nose, explaining the discrepancy. Additionally, all cases show a sharp transition between low (<8%) to higher (10-15%) relative errors along the projectile's cylinder region. The exact location varies between flow cases, advancing downstream with Mach

number, however, in all result sets the error dominates the entire flow region and then fades towards the projectile's boattail. This is visible in the filled contours as a visible transition between compressed flow to freestream density between the bow shock and the first expansion fan. The error is more pronounced at the highest speed, and lowest at Mach 2.0. Nevertheless, an equivalent transition is not perceptible in the pixel displacement fields, suggesting the artifact is introduced by the inverse Abel integral computation. The remaining field regions differ by less than 10% with the CFD solutions.

As further validation of the CFD methodology, the drag coefficient grid convergence is presented against the experimentally measured drag coefficients for the Mach 2.50 flow case in Table 2.

Table 2 Grid Convergence Study of the 4.5:1 scale NATO 5.56 M855 drag coefficient at Mach 2.5 and comparison with wind tunnel experiments and live firings [4]

Cells $\times 10^7$	C_D	r_{mesh}	GCI, %	ϵ_{approx}, %	ϵ_{extrp}, %	$C_{D,\text{extrp}}$	$C_{D,\text{exp}}$	$C_{D,\text{Silton}}$
3.704	0.2371	1.53	0.59	0.56	0.36	0.2362	0.2569	0.3103
1.038	0.2384	1.50	1.15	1.03	0.93	**Base flow corrections**		
0.3079	0.2409	1.54	2.37	2.31	2.10	0.2859	0.3066	
0.0849	0.2466							

The initial mesh was progressively refined in the test-section volume, projectile and sting surfaces, and wake region. A representative mesh size was calculated in each case and tracked between refinements to ensure a refinement ratio $r_{\text{mesh}} > 1.3$[36]. The final drag coefficient was calculated using Richardson extrapolation and taking all cases into account, resulting in a value of 0.2362 and an associated Grid Convergence Index (GCI) of 0.59%. The experimental drag coefficient was obtained by normalising the measured force with the test section Mach number. The force signal was averaged over a 3-second window after the start-up pressure fluctuations had settled. The numerical result underpredicts the experimental value of 0.2569 by 8.06%. To account for sting interference, the base drag correction from [37] is added, assuming a nominally uniform pressure distribution over the projectile base. The corrected coefficients agree within 1.2% (experimentally) and 16.6% (numerically) with a quadratic fit of the live firing data from [4] at the same Mach number.

C. CNN Procedure

1. Training Data

The training data for the CNN was generated using the Taylor-Maccoll solver described in Section III.B.3. A total of 1377 data samples were created, including normalised density, pressure, temperature, axial and radial velocity fields, and a label array including absolute free-stream values. The flow cases ranged between Mach 1.20 and 5.0, and shock angles between 1 and 80 degrees, where non-physical results were automatically discarded. The resulting cone angles varied with Mach number to satisfy the imposed shock angles, resulting in different geometries amongst the dataset. To improve generality, the physical grid was transformed into a square computational domain via the coordinate transformations:

$$x(\xi) = \xi \tag{6}$$

$$r(\xi, \eta) = r_{\text{surf}}(\xi) + \eta(1 - r_{\text{surf}}(\xi)) \tag{7}$$

$$r_{\text{surf}}(\xi) = \begin{cases} \xi \tan(\theta_c), & \text{if } \xi > 0 \\ 0, & \text{otherwise} \end{cases} \tag{8}$$

where x and y are the axial and radial physical coordinates, ξ and η are the axial and radial computational coordinates, r_{surf} is the radial coordinates along the symmetry axis ($r = 0$) and cone surface and θ_c is the cone angle. The physical and computational grids were created as Pytorch tensors [38], allowing for exact computations of the grid metrics and Jacobian determinant using the built-in automatic differentiation functions. The grid transformation is shown in Figure 9. The model input data is a multichannel tensor with the normalised density field and computational coordinates and the outputs are the four remaining scalar fields.

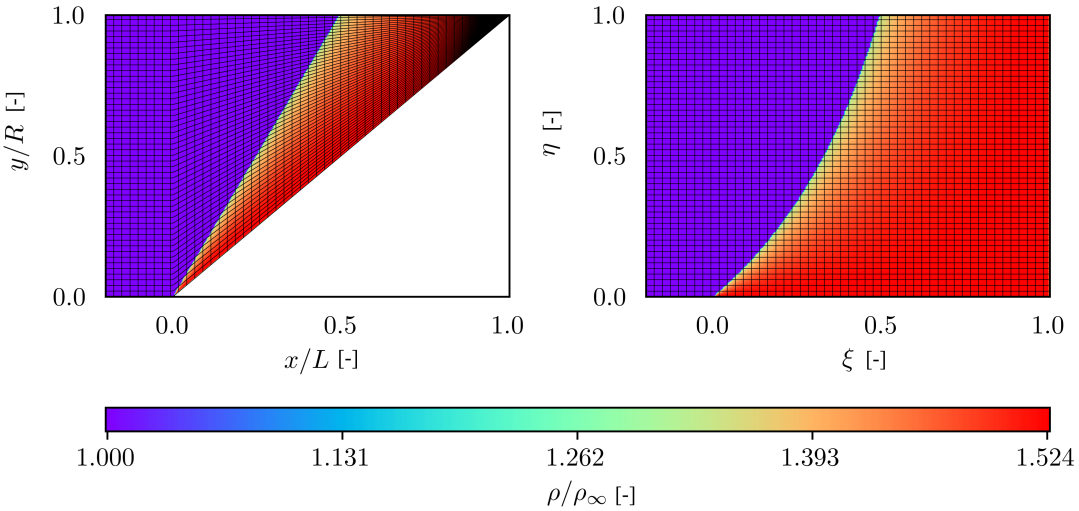

Fig. 9 Physical (left) and computational (right) grids with normalised density contours for a Mach 2.50 flow over a 15 degree cone. Every 5th mesh point is plotted for clarity.

2. Physics informing

To extend the model's predictive capability outside the numerical data, the steady, inviscid axisymmetric mass, axial and radial momentum conservation equations were implemented to construct a purely physical cost function. In addition, Dirichlet boundary conditions were specified at the inlet and symmetry boundaries, and a Neumann boundary condition was assigned to the top boundary for all fields. A velocity tangency condition was applied over the cone surface. The resulting loss functions are:

$$\mathcal{L}_{\text{mass}} = \frac{1}{N_{\text{int}}} \sum_{i=1}^{N_{\text{int}}} \left(\frac{\partial(\rho_i^* u_i^*)}{\partial x_i} + \frac{\partial(\rho_i^* v_i^*)}{\partial r_i} + \frac{\rho_i^* v_i^*}{r_i} \right)^2 \tag{9}$$

$$\mathcal{L}_{\text{axial}} = \frac{1}{N_{\text{int}}} \sum_{i=1}^{N_{\text{int}}} \left(\frac{\partial(\rho_i^* u_i^{*2})}{\partial x_i} + \frac{\partial(\rho_i^* u_i^* v_i^*)}{\partial r_i} + \frac{\rho_i^* u_i^* v_i^*}{r_i} + \frac{1}{\gamma M_\infty^2} \frac{\partial p_i^*}{\partial x_i} \right)^2 \tag{10}$$

$$\mathcal{L}_{\text{radial}} = \frac{1}{N_{\text{int}}} \sum_{i=1}^{N_{\text{int}}} \left(\frac{\partial(\rho_i^* u_i^* v_i^*)}{\partial x_i} + \frac{\partial(\rho_i^* v_i^{*2})}{\partial r_i} + \frac{\rho_i^* v_i^{*2}}{r_i} + \frac{1}{\gamma M_\infty^2} \frac{\partial p_i^*}{\partial r_i} \right)^2 \tag{11}$$

$$\mathcal{L}_{\text{boundary}} = \frac{1}{N_{\text{bc}}} \sum_{j=1}^{N_{\text{bc}}} \left\| q_j - \hat{q}_j \right\|^2 \tag{12}$$

where the $*$ values denote freestream normalised quantities, ρ, u, v, p represent the density, axial, and radial velocity components, and pressure, M_∞ is the free-stream Mach number, γ is the ratio of specific heats, N_{int} is the number of interior points, N_{bc} are the boundary points and q and $\hat{q}$ are the predicted and target boundary conditions. The physical derivatives are evaluated using the exact metric terms using convolution operations with central difference kernels. Each contributing loss term is weighted such that residuals were of order of magnitude 1, to prevent the network from over-optimizing a particular equation over the rest. The resulting weighing factors were 1×10^{-5}, 1×10^{-4}, 1×10^{-4}, and 1×10^{-2} for mass, axial momentum, radial momentum and boundary loss respectively.

Now, we focus on the main roadblock impeding the network's performance. To illustrate this, the pointwise residual maps for the three conservation loss terms are shown in Figure10 for a Mach 2.50 flow over a 15-degree cone target field, i.e. a direct output from the numerical solver. In all cases, the residuals are near zero upstream of the shock region, as would be expected. Similarly, the conservation laws are well obeyed away from the cone tip within the compression

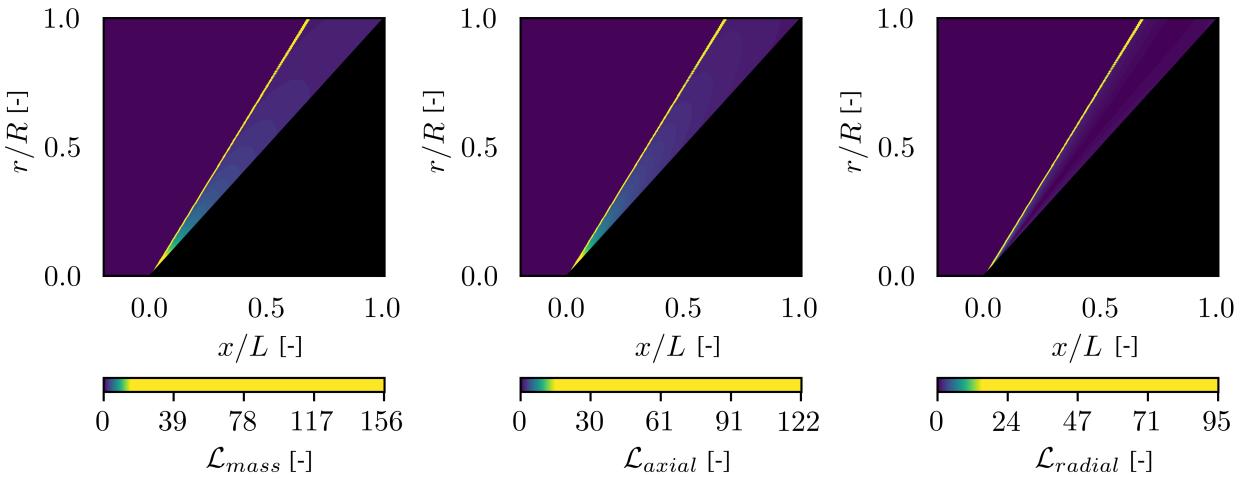

Fig. 10 Physics losses on the numerical solution of a Mach 2.50 flow over a 15 degree cone (a) mass (b) axial momentum (c) radial momentum

region. However, moderate residuals are observed near the cone tip due to the grid introduced error increasing as the gradients steepen. Most importantly, large violations of the loss terms are observed over the thin shockwave region. This sharp shock-induced gradient results in an overall significant loss in the ground-truth case. The model was observed to minimise the loss on the training and validation data below said ground-truth loss, but nevertheless, this resulted in ignoring the shock and hence unphysical predictions. Further improvements to the loss treatment are required to provide a way of mapping the shock location and adapting the weights around this region.

3. Data-Driven Results

The model was also trained with physics loss weights set to zero, only relying on a mean squared error (MSE) data loss cost function. The model outputs and MSEs with the target fields after 1000 epochs of training are presented in Figure 11. The flow case shown is for a Mach 2.55 flow over a 15.2-degree cone, since the exact experimental conditions (Mach 2.5 flow and 15-degree cone) were not explicitly included in the dataset. In all cases, values outside of ± 1% the minimum and maximum of the fields are masked to the respective upstream quantities for clear visualization. The normalised pressure and temperature fields show excellent agreement over the majority of the domain, with a clear capture of the shock discontinuity location. The error contours show a near-zero loss in the free field and post-shock regions, with predictions of similar accuracy for the temperature field along the discontinuity. The model's radial velocity output shows larger discrepancies with the numerical results, with an MSE of around 0.08. Noticeably, the axial velocity component is poorly predicted over practically the entire post-shock region, with large error values of 0.2-0.4 throughout. Other peaks in the error are visible across all fields in localised near-wall pockets, beyond $x/L \gtrsim 0.269$. A similar pattern is observed amongst all test cases in the dataset.

Despite the shortcomings of the exclusively data-driven predictions, particularly on the velocity fields, the pressure and temperature variables are predicted with enough accuracy to expect reasonable predictions for an experimentally obtained BOS density result. However, after evaluating the model on the experimental density results, the predictions were non-physical and so are not presented here. This result implies the need of additional physical constraints to translate the model to data samples truly outside the training sets.

V. Conclusions and Future Work

In this work, we have investigated the use of axisymmetric background-oriented schlieren (BOS) on the Mach 1.50, 2.0, and, 2.50 flow over a scaled NATO 5.56 mm M855 projectile across several Mach numbers, as well as a 15° cone at Mach 2.5. We implemented a reconstruction method for recovering density fields from BOS displacement maps and noted a practical approach to improve camera alignment based on analysis of the vertical displacement component.

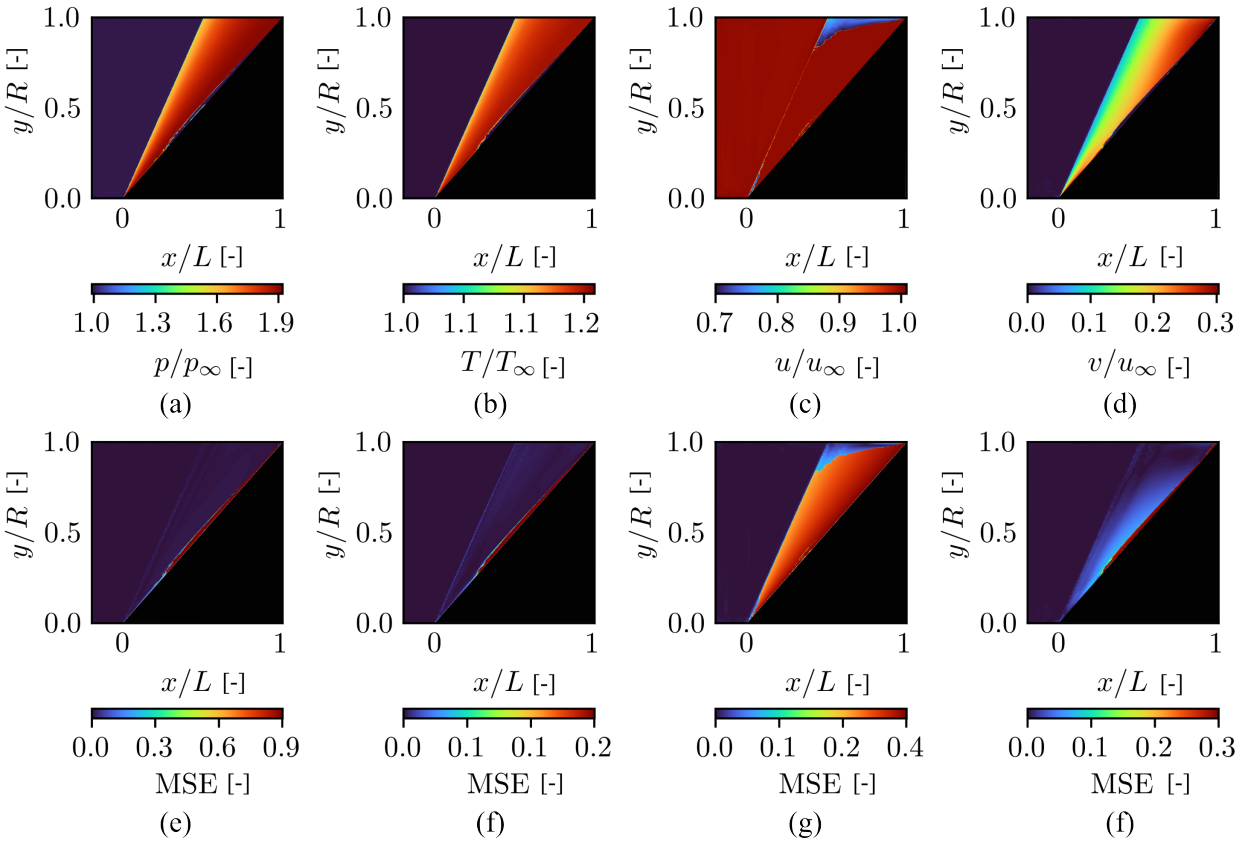

Fig. 11 Data model outputs (top) and MSE errors relative to the Taylor-Maccoll numerical solution (bottom) over a 15.2 degree cone at Mach 2.55. Values outside of ±1% of the minimum and maximum field values are masked to the freestream quantities for visual comparison. (a)(e) pressure (b)(f) temperature (c)(g) axial velocity (d)(f) radial velocity

To evaluate the cone flow, we implemented a Taylor–Maccoll solver to provide a theoretical comparison, and a wind tunnel RANS CFD model for the projectile configurations. Across all test cases, predictions from the BOS-based reconstruction remained within 15% error globally and within 10% over most of the domain. The primary discrepancies were concentrated near shocks, expansion fans, and near model regions, including the stagnation point, where BOS resolution is reduced due to blurring. A force balance was used to experimentally estimate the drag coefficient at Mach 2.50 and provide further validation to the CFD model, showing an agreement with live-firing data of 1.2%, 8.1% error between CFD and force balance, and 16.6% between CFD and live fire.

Next, we trained a custom U-Net architecture to infer pressure, temperature, and velocity components from grid-transformed density field inputs. Initially, we applied a physics-only loss based on the axisymmetric conservation of mass, momentum, and boundary conditions, which proved unsuccessful due to large localised residuals around the shock and stagnation point regions, introduced by grid interpolation. Finally, a purely data-driven model was trained, which produced good predictions for pressure and temperature, moderate accuracy for radial velocity, and poor results for axial velocity. The model failed to produce physical results from an experimental density input, revealing the need for additional physics-based constraints.

Future work will focus on improving the robustness and physical consistency of the model's predictions, potentially applying further treatment to the experimental inputs. Furthermore, we will incorporate shock-aware masking or adaptive loss weighting in the neural network to prevent sharp discontinuities from dominating the training process and distorting gradients in smooth regions. Finally, integrating complementary measurement techniques like Pressure-Sensitive Paint

could help resolve near-wall pressure fields more accurately, overcoming some of the limitations of blurring, and further contributing to the goal of drag coefficient predictions from image data.

VI. Acknowledgements

Data cannot be shared due to commercial restrictions. For the purposes of open access, the authors have applied a Creative Commons Attribution (CC BY) licence to any Accepted Author Manuscript version arising from this submission.

References

[1] McCoy, R. L., *Modern exterior ballistics: the launch and flight dynamics of symmetric projectiles*, rev. 2. ed ed., Schiffer Publ, Atglen, Pa, 2012.

[2] Army Materiel Command Alexandria VA, *Engineering Design Handbook. Design for Control of Projectile Flight Characteristics.*, 1966.

[3] Robert L. McCoy, "The aerodynamic characteristics of .50 ball, M33, API, and APIT, M20 ammunition," Tech. Rep. BRL-MR-3810, US Army Ballistics Research Laboratory, Aberdeen Proving Ground, MD, 21005-5066, Jan. 1990.

[4] Silton, S. I., and Howell, B. E., "Aerodynamic and Flight Dynamic Characteristics of 5.56-mm Ammunition: M855:," Tech. rep., Defense Technical Information Center, Fort Belvoir, VA, May 2010. https://doi.org/10.21236/ADA530895, URL http://www.dtic.mil/docs/citations/ADA530895.

[5] P. Plostins, Robert L. McCoy, and Barbara A. Wagoner, "Aeroballistic Performance of the 25mm M910 TPDS-T Range Limited Training Projectile," Tech. rep., US Army Ballistics Research Laboratory, Aberdeen Proving Ground, MD, 21005-5066, Jan. 1991.

[6] de Briey, V., "Small-Caliber Exterior Ballistics : Aerodynamic Coefficients Determination by CFD," Ph.D. thesis, 2021.

[7] Escudero, M. A., Marinus, B., Depuru-Mohan, K., and De Briey, V., "Scale Effects on the Zero Yaw Drag Coefficient of Small Caliber Projectiles at Mach 2," *AIAA AVIATION FORUM AND ASCEND 2024*, American Institute of Aeronautics and Astronautics, Las Vegas, Nevada, 2024. https://doi.org/10.2514/6.2024-4525, URL https://arc.aiaa.org/doi/10.2514/6.2024-4525.

[8] Nietubicz, C. J., and Opalka, Klaus O, "Supersonic wind tunnel measurements of static and Magnus aerodynamic coefficients for projectile shapes with tangent and secant ogive noses," Memorandum report ARBRL-MR-02991, US Army Ballistics Research Laboratory, Aberdeen Proving Ground, MD, 21005-5066, Feb. 1980.

[9] Moumen, A., Grossen, J., Ndindabahizi, I., Gallant, J., and Hendrick, P., "Visualization and analysis of muzzle flow fields using the Background-Oriented Schlieren technique," *Journal of Visualization*, Vol. 23, No. 3, 2020, pp. 409–423. https://doi.org/10.1007/s12650-020-00639-w, URL http://link.springer.com/10.1007/s12650-020-00639-w.

[10] Cakir, B. O., Grossir, G., Saracoglu, B., and Fureby, C., "Numerical and experimental investigations of flow features over a wedge exposed to supersonic flow at high Reynolds numbers," *Physics of Fluids*, Vol. 36, No. 7, 2024, p. 076112. https://doi.org/10.1063/5.0216479, URL https://pubs.aip.org/pof/article/36/7/076112/3303107/Numerical-and-experimental-investigations-of-flow.

[11] Raissi, M., Perdikaris, P., and Karniadakis, G., "Physics-informed neural networks: A deep learning framework for solving forward and inverse problems involving nonlinear partial differential equations," *Journal of Computational Physics*, Vol. 378, 2019, pp. 686–707. https://doi.org/10.1016/j.jcp.2018.10.045, URL https://linkinghub.elsevier.com/retrieve/pii/S0021999118307125.

[12] Mao, Z., Jagtap, A. D., and Karniadakis, G. E., "Physics-informed neural networks for high-speed flows," *Computer Methods in Applied Mechanics and Engineering*, Vol. 360, 2020, p. 112789. https://doi.org/10.1016/j.cma.2019.112789, URL https://linkinghub.elsevier.com/retrieve/pii/S0045782519306814.

[13] Molnar, J. P., Venkatakrishnan, L., Schmidt, B. E., Sipkens, T. A., and Grauer, S. J., "Estimating density, velocity, and pressure fields in supersonic flows using physics-informed BOS," *Experiments in Fluids*, Vol. 64, No. 1, 2023, p. 14. https://doi.org/10.1007/s00348-022-03554-y, URL https://link.springer.com/10.1007/s00348-022-03554-y.

[14] Molnar, J. P., Grauer, S. J., Léon, O., Donjat, D., and Nicolas, F., "Physics-Informed Background-Oriented Schlieren of Turbulent Underexpanded Jets," *AIAA SCITECH 2023 Forum*, American Institute of Aeronautics and Astronautics, National Harbor, MD & Online, 2023. https://doi.org/10.2514/6.2023-2441, URL https://arc.aiaa.org/doi/10.2514/6.2023-2441.

[15] Molnar, J. P., Davami, J., Juliano, T. J., Sidharth, G. S., Yang, X. I., and Grauer, S. J., "Reconstructing Hypersonic Flow Over a Bluff Body from Experimental Background-Oriented Schlieren Data," *AIAA SCITECH 2024 Forum*, American Institute of Aeronautics and Astronautics, Orlando, FL, 2024. https://doi.org/10.2514/6.2024-2493, URL https://arc.aiaa.org/doi/10.2514/6.2024-2493.

[16] Rohlfs, L., and Weiss, J., "Assimilating mean velocity fields of a shockwave–boundary layer interaction from background-oriented schlieren measurements using physics-informed neural networks," *Physics of Fluids*, Vol. 36, No. 7, 2024, p. 076134. https://doi.org/10.1063/5.0208040, URL https://pubs.aip.org/pof/article/36/7/076134/3305484/Assimilating-mean-velocity-fields-of-a-shockwave.

[17] Wang, X., Wang, H., Wang, N., Chen, X., and Liu, X., "Super-resolution reconstruction of background-oriented Schlieren displacement field based on the convolution neural network with the gradient loss function," *Measurement Science and Technology*, Vol. 35, No. 10, 2024, p. 106002. https://doi.org/10.1088/1361-6501/ad4dc2, URL https://iopscience.iop.org/article/10.1088/1361-6501/ad4dc2.

[18] Mucignat, C., Manickathan, L., Shah, J., Rösgen, T., and Lunati, I., "A lightweight convolutional neural network to reconstruct deformation in BOS recordings," *Experiments in Fluids*, Vol. 64, No. 4, 2023, p. 72. https://doi.org/10.1007/s00348-023-03618-7, URL https://link.springer.com/10.1007/s00348-023-03618-7.

[19] Zhao, X., Gong, Z., Zhang, Y., Yao, W., and Chen, X., "Physics-informed convolutional neural networks for temperature field prediction of heat source layout without labeled data," *Engineering Applications of Artificial Intelligence*, Vol. 117, 2023, p. 105516. https://doi.org/10.1016/j.engappai.2022.105516, URL https://linkinghub.elsevier.com/retrieve/pii/S0952197622005061.

[20] Zhang, Z., "A physics-informed deep convolutional neural network for simulating and predicting transient Darcy flows in heterogeneous reservoirs without labeled data," *Journal of Petroleum Science and Engineering*, Vol. 211, 2022, p. 110179. https://doi.org/https://doi.org/10.1016/j.petrol.2022.110179, URL https://www.sciencedirect.com/science/article/pii/S0920410522000705.

[21] Grimm, V., Heinlein, A., and Klawonn, A., "Learning the solution operator of two-dimensional incompressible Navier-Stokes equations using physics-aware convolutional neural networks," *arXiv preprint arXiv:2308.02137*, 2023. URL https://doi.org/10.48550/arXiv.2308.02137.

[22] Lee Hammer, R., and D. Leff, A., "Linear Aerodynamic Loads on Cone-Cylinders at Mach Numbers from 0.7 to 2.0," NASA Contractor Report NASA CR-413, Locheed Missiles and Space Company, Huntsville, Alabama, March 1966.

[23] Siemens Digital Industries Software, "Simcenter STAR-CCM+, version 2310," , 2023.

[24] Menter, Florian R., "Improved two-equation k-omega turbulence models for aerodynamic flows," Technical memorandum NASA-TM-103975, NASA Ames Research Center, Moffet Field, CA, United States, Oct. 1992.

[25] Spalart, P., and Allmaras, S., "A one-equation turbulence model for aerodynamic flows," *30th Aerospace Sciences Meeting and Exhibit*, American Institute of Aeronautics and Astronautics, Reno,NV,U.S.A., 1992. https://doi.org/10.2514/6.1992-439, URL https://arc.aiaa.org/doi/10.2514/6.1992-439.

[26] G. Cross, P., and R. West, M., "Simulation of Hypersonic Flow Using STAR-CCM+," Technical Report NAWCWD TM 8824, Naval Air Warfare Center Weapons Division, Naval Air Warfare Center Weapons Division, 1 Administration Circle, China Lake, California, 93555-6100, January 2019.

[27] Farnebäck, G., "Two-Frame Motion Estimation Based on Polynomial Expansion," 2003, pp. 363–370. https://doi.org/10.1007/3-540-45103-X_50.

[28] Bradski, G., "The OpenCV Library," *Dr. Dobb's Journal of Software Tools*, 2000.

[29] Moumen, A., Laboureur, D., Gallant, J., and Hendrick, P., "A new approach for the reconstruction of axisymmetric refractive index fields from background-oriented schlieren measurements," *Shock Waves*, Vol. 32, No. 3, 2022, pp. 313–318. https://doi.org/10.1007/s00193-022-01071-9, URL https://link.springer.com/10.1007/s00193-022-01071-9.

[30] Venkatakrishnan, L., and Meier, G. E. A., "Density measurements using the Background Oriented Schlieren technique," *Experiments in Fluids*, Vol. 37, No. 2, 2004, pp. 237–247. https://doi.org/10.1007/s00348-004-0807-1, URL http://link.springer.com/10.1007/s00348-004-0807-1.

[31] Pretzier, G., "A New Method for Numerical Abel-Inversion," *Zeitschrift für Naturforschung A*, Vol. 46, No. 7, 1991, pp. 639–641. https://doi.org/10.1515/zna-1991-0715, URL https://www.degruyter.com/document/doi/10.1515/zna-1991-0715/html.

[32] Lam, S. K., Pitrou, A., and Seibert, S., "Numba: a LLVM-based Python JIT compiler," *Proceedings of the Second Workshop on the LLVM Compiler Infrastructure in HPC*, ACM, Austin Texas, 2015, pp. 1–6. https://doi.org/10.1145/2833157.2833162, URL https://dl.acm.org/doi/10.1145/2833157.2833162.

[33] Anderson, J. D., *Modern compressible flow: with historical perspective*, 3rd ed., McGraw-Hill series in aeronautical and aerospace engineering, McGraw-Hill, Boston, Mass., 2003.

[34] Ronneberger, O., Fischer, P., and Brox, T., "U-Net: Convolutional Networks for Biomedical Image Segmentation," *arXiv preprint arXiv:1505.04597*, 2015. https://doi.org/10.48550/arXiv.1505.04597.

[35] Kingma, D. P., and Ba, J., "Adam: A Method for Stochastic Optimization," *arXiv preprint arXiv:1412.6980*, 2014. URL https://arxiv.org/abs/1412.6980.

[36] Roache, P. J., "Perspective: A Method for Uniform Reporting of Grid Refinement Studies," *Journal of Fluids Engineering*, Vol. 116, No. 3, 1994, pp. 405–413. https://doi.org/10.1115/1.2910291, URL https://asmedigitalcollection.asme.org/fluidsengineering/article/116/3/405/411554/Perspective-A-Method-for-Uniform-Reporting-of-Grid.

[37] Ballistic Research Laboratories, "Supersonic Wind Tunnel Tests of Small Caliber Projectiles: Cal. .50 API M23; Cal. .60 API T39; and 20mm HEI M97," Technical Note AD693249, Ballistic Research Laboratories, Aberdeen Proving Ground, MD 21005, June 1949.

[38] Paszke, A., Gross, S., Massa, F., Lerer, A., Bradbury, J., Chanan, G., Killeen, T., Lin, Z., Gimelshein, N., Antiga, L., Desmaison, A., Köpf, A., Yang, E., DeVito, Z., Raison, M., Tejani, A., Chilamkurthy, S., Steiner, B., Fang, L., Bai, J., and Chintala, S., "PyTorch: An Imperative Style, High-Performance Deep Learning Library," , 2019. https://doi.org/10.48550/arXiv.1912.01703, URL https://arxiv.org/abs/1912.01703.

https://dspace.org/

Supersonic projectile flow field reconstruction using background oriented schlieren and physics informed convolutional neural networks

Escudero, Miguel A.; Marinus, Benoît G.; Depuru-Mohan, Karthik; Debiasi, Marco; Saddington, Alistair J.

2025-07-25
American Institute of Aeronautics and Astronautics (AIAA)
https://doi.org/10.2514/6.2025-3198
Escudero MA, Marinus BG, Depuru-Mohan K, et al., (2025) Supersonic projectile flow field reconstruction using background oriented schlieren and physics informed convolutional neural networks. In: AIAA Aviation Forum and Ascend 2025, 21-25 July 2025, Las Vegas, Nevada, Article number AIAA 2025-3198

Downloaded from a DSpace repository. https://dspace.org/